

Article

The NiCo Bimetal Catalyst Loaded on Polyvinylidene Fluoride Coated on the Self-Supporting Silk Electrode as an Advanced Electrocatalyst for the Hydrogen Evolution Reaction

Haoyu Wang ^{1,2}, Chunyong Zhang ^{1,2,*} , Zhe Li ¹, Yinpin Wen ² and Li Shu ²

¹ School of Chemistry and Environmental Engineering, Jiangsu University of Technology, Changzhou 213001, China; 2021657055@smail.jsut.edu.cn (H.W.); 2021657032@smail.jsut.edu.cn (Z.L.)

² Jiangsu Key Laboratory of Precious Metal Chemistry and Technology, Jiangsu University of Technology, Changzhou 213001, China; wenyp@jsut.edu.cn (Y.W.); shuli@jsut.edu.cn (L.S.)

* Correspondence: zhangcy@jsut.edu.cn

Abstract: In this work, a Ni_xCo_x/Silk-PVDF bimetallic catalyst electrode was prepared for the hydrogen evolution reaction (HER) in hydropower. This cheap, durable, and efficient electrode has good practical application prospects. Green natural silk, which will pollute the environment. The electrodes (obtained by varying the Ni:Co ratio and hydrothermal times) were prepared hydrothermally. Ni and Co elements were revealed by X-ray diffraction, X-ray photoelectron spectroscopy, and transmission electron microscopy. Ni₂Co₂/silk-PVDF was identified as an effective catalyst in 1 M KOH alkaline electrolyte with an overpotential of 89.4 mV at 20 mA cm⁻² and a Tafel slope of 47.46 mv dec⁻¹. It showed low resistance and a high specific surface area in EIS and CV tests, respectively, proving its superior HER performance. Finally, the stability and durability of the electrode coated with PVDF were demonstrated via testing at a voltage of -0.1 V over 24 h. This work provides an environmentally friendly and simple method to load metal on a self-supporting electrode to be used in the hydrogen evolution reaction.



Citation: Wang, H.; Zhang, C.; Li, Z.; Wen, Y.; Shu, L. The NiCo Bimetal Catalyst Loaded on Polyvinylidene Fluoride Coated on the Self-Supporting Silk Electrode as an Advanced Electrocatalyst for the Hydrogen Evolution Reaction. *Catalysts* **2023**, *13*, 987. <https://doi.org/10.3390/catal13060987>

Academic Editors: Umut Aydemir and Naemeh Sadat Peighambaroust

Received: 30 April 2023
Revised: 26 May 2023
Accepted: 5 June 2023
Published: 9 June 2023



Copyright: © 2023 by the authors. Licensee MDPI, Basel, Switzerland. This article is an open access article distributed under the terms and conditions of the Creative Commons Attribution (CC BY) license (<https://creativecommons.org/licenses/by/4.0/>).

Keywords: silk; PVDF; bimetallic electrocatalyst; electrochemical; HER

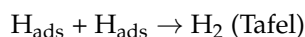
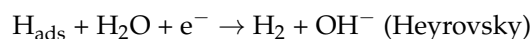
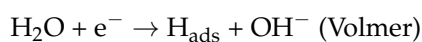
1. Introduction

With the development of science and technology and the study of basic theories, the James Webb Space Telescope is a milestone in the human exploration of deep space. In order to launch it into orbit, the rocket carrying it is extremely important. Today, all rockets worldwide, without exception, use chemical fuel, which is generally composed of liquid oxygen and liquid hydrogen. Due to the highly active chemical properties of hydrogen, liquid hydrogen has a large calorific value. In addition, it has a higher specific impulse, which is an indicator that measures the combustion efficiency of a rocket; the higher the specific impulse value, the greater the impulse generated by consuming the same mass of fuel and the greater the acceleration of the rocket. The combination of liquid hydrogen and oxygen has a specific impulse of over 400 [1,2]. For highly pure hydrogen, the industry usually uses hydroelectrolysis (hydrogen evolution), a green and economical method of converting electrical energy into chemical energy [3].

Nowadays, some precious metal-based materials and their alloys are considered to be ideal electrocatalysts for the HER process [4]. However, due to the low output and high preparation cost of these rare metals, they have been unable to be used as the most cost-effective electrocatalysts. Therefore, it is necessary to find electrocatalysts with high activity and low cost that are environmentally sound and rich in earth to replace the above precious metals. Thus far, a variety of low-cost alternatives to catalytic HER have been studied, including metal oxides, chalcogenides, phosphates, and perovskites [5–11]. Atchudan's study used *Anacardium occidentale* nut's skin to product the porous carbon material. The

Anacardium occidentale nut's skin is convenient to get at a low cost [12]. Many authors have utilized natural green biowastes/biomass for the synthesis of carbon materials [13,14].

The method of hydrogen production via the electrolysis of water has developed rapidly in recent years, and the technology is now more mature than traditional methods. Its raw material is water, the reaction process is clean and environmentally friendly, and there is no carbon dioxide in the product. Water electrolysis will not aggravate the greenhouse effect, and the entire process is very much in line with the concept of sustainable development. Therefore, it is a feasible and mainstream method for carrying out HER from electrolytic water to prepare hydrogen. The electrolytic water reaction is divided into two semi-reactions: the hydrogen evolution reaction and the oxygen evolution reaction [15–20]. The cathode HER for the production of high-purity hydrogen is a reaction based on a two-electron transfer process. In the alkaline solution, HER is divided into Volmer, Heyrovsky, and Tafel steps, through which hydrogen atoms are adsorbed or desorbed [21,22]. The specific reactions are as follows:



Thus far, it has been reported that the number of HER catalysts in an alkaline medium is less than that in an acidic medium. In an alkaline medium, HER commercial catalysts mainly use platinum groups, such as Pt, Pd, etc. [23]. However, these are precious metals, which are not only a scarce resource but also expensive; therefore, the use of transition metals instead of precious metals is now an important replacement for commercial catalysts. Compared with the platinum group, transition metals, for example Ni, Co, Fe, Cu, etc. [20,24], may have good hydrogen spillover properties under certain conditions [25]. In addition, studies have shown that bimetallic compounds have stronger electrochemical performance than single metal compounds, which can bring better electrochemical performance to HER. In recent years, because of the synergistic effect between the catalytic properties of Ni and Co, Ni has become known for its low HER overpotential, whereas Co has become known for its high hydrogen adsorption. Research on Ni and Co has steadily increased because their hydrogen production activity is equivalent to that of precious metal catalysts [26–29].

In ancient China, silk is made into yarn and textiles on a large scale in the textile industry. The Silk Road was a land-based trade route from China through Central Asia to South and West Asia, as well as Europe and North Africa. Silk has good mechanical properties, controlled biodegradability, and novel dielectric properties due to the development of manufacturing technology and research on the structure of silk. Silk is a well-known natural biomaterial. It has been processed into various materials such as nanofibers, flexible films, hydrogels, and 3D porous aerogels. Therefore, this study used silk as a self-supporting electrode.

Here, a NiCo bimetallic catalyst was synthesized using a simple and green solvothermal route. This study used waste silk as the self-supporting electrode on which the NiCo bimetal was loaded. PVDF was used to coat the substrate of the silk electrode, which increases the mechanical strength and durability for working stability in electrochemistry. The Ni and Co metals were loaded directly on silk via hydrothermal synthesis twice and grown uniformly on the silk surface to ensure maximum electrochemically active surface area. Under the same metal load mass and conditions, metals Ni, Co, and NiCo were loaded on four different electrodes separately as the control groups. Further, the four different electrodes were used as four different electrocatalysts for HER in the alkaline solution (1 M KOH). The crystal structure, physicochemical properties, and electrochemical performance of the prepared samples were tested using various analytical instruments. The HER reaction was monitored by cyclic voltammetry, electrochemically active surface area,

electrochemical impedance spectroscopy, linear sweep voltammetry, long-term stability and Tafel methods. Their applicability as HER electrocatalysts was studied.

2. Results and Discussion

2.1. Physicochemical Properties of the $Ni_xCo_x/Silk-PVDF$ Electrodes

The strategy used for the synthesis of $Ni_xCo_x/Silk-PVDF$ electrodes is illustrated in Figure 1a. The waste silk was yellowish brown after being wrapped with PVDF. Subsequently, the final sample prepared by hydrothermal synthesis appeared brown and had purple powder on the surface. In Figure 1b,c the SEM images show the overlapping of the metal elements, where octahedral particles were attached to the surface of the silk. In Figure 1c–e, the metal Ni was uniformly distributed on the surface of the silk, while the metal Co was attached to the surface of the silk in an octahedral form (Figure 1d,e show the distribution of the Ni and Co elements, respectively). The molar mass ratio of Ni and Co used in the experiment was 50:50. According to Figure 1f, the mass percentage of Ni and Co was close to 50:50, which conforms to the experimental rule.

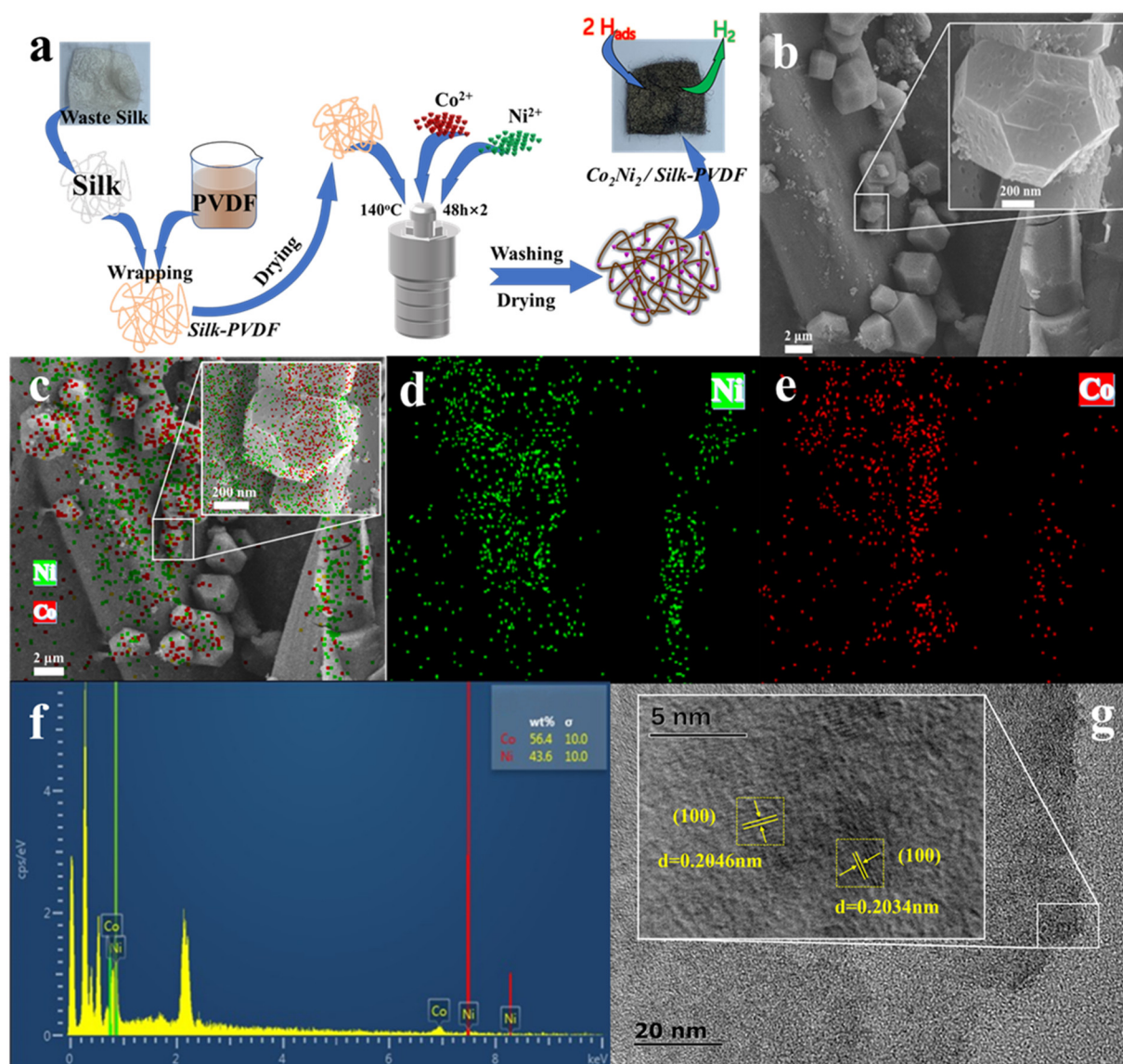


Figure 1. Synthesis process of the $Ni_2Co_2/Silk-PVDF$ electrode by simple solvothermal and their eco-friendly energy applications (a), SEM image (b), overlapping of all the metal elements (c), EDS element mappings of the $Ni_2Co_2/Silk-PVDF$ electrode (d–f), and TEM images of the $Ni_2Co_2/Silk-PVDF$ electrode (g).

The morphology and fine structure of $\text{Ni}_2\text{Co}_2/\text{Silk-PVDF}$ were further observed using TEM images (Figure 1g). The TEM images show that the lattice fringes of the Co (111) layer were clear, and the spacing of the lattice fringe was 0.2046 nm [30], which is very close to the properties of metal Co. The lattice fringes of (111) Ni were also clear [31], and the spacing of the lattice fringe was about 0.2034 nm, which is close to the value characteristic of metal Ni.

Figure 2 shows the XRD patterns of the $\text{Ni}_x\text{Co}_x/\text{Silk-PVDF}$ electrodes synthesized through the hydrothermal process. All the $\text{Ni}_x\text{Co}_x/\text{Silk-PVDF}$ sample electrodes showed a distinct diffraction peak similar to Silk-PVDF between 18° and 26° ; the XRD patterns of silk fibroin were determined in previous studies to have the specific silk II peak at 20.2° and silk I peak at 24.5° [32–34]. This is due to the fact that the amorphous diffraction peak of the silk and the four diffraction peaks of α -PVDF are formed by overlapping each other; due to the minimal amount of PVDF wrapping, the diffraction peaks of α -PVDF were not obvious [35]. In general, the primary diffraction peaks of Co and Ni appear at $2\theta = 44.4^\circ$, 51.6° , and 76.1° (PDF#00-001-1255 for Co and PDF#00-001-1258 for Ni) [36–38]. Next, the Co/Silk-PVDF, Ni/Silk-PVDF, $\text{Ni}_1\text{Co}_1/\text{Silk-PVDF}$, and $\text{Ni}_2\text{Co}_2/\text{Silk-PVDF}$ samples were compared with the Silk-PVDF sample. The difference was that there were (111), (200), and (220) diffraction peaks corresponding to the two metals. In the four cases of the $\text{Ni}_x\text{Co}_x/\text{Silk-PVDF}$ electrodes, the corresponding diffraction peaks of the NiCo bimetal were almost the same as those of the single Ni or Co metal. Lastly, when the Co/Silk-PVDF and Ni/Silk-PVDF samples were compared with the $\text{Ni}_1\text{Co}_1/\text{Silk-PVDF}$ and $\text{Ni}_2\text{Co}_2/\text{Silk-PVDF}$ samples, the diffraction peak intensity of the bimetal synthesis was obviously due to that of the single metal synthesis. Furthermore, in the case of the same quality of loaded metal, the corresponding diffraction peaks of the $\text{Ni}_x\text{Co}_x/\text{Silk-PVDF}$ electrocatalysts became sharp and narrow with an increasing number of syntheses.

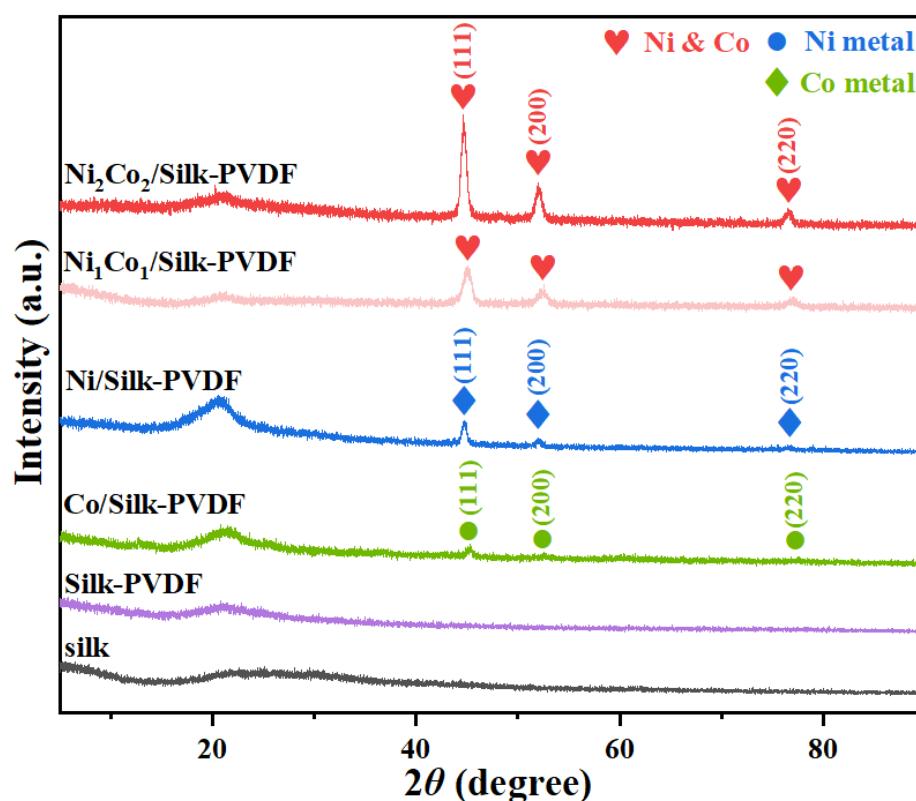


Figure 2. XRD patterns of the $\text{Ni}_x\text{Co}_x/\text{Silk-PVDF}$ electrodes.

Figure 3a presents the XPS survey spectrum for $\text{Ni}_2\text{Co}_2/\text{Silk-PVDF}$, also confirming the presence of the Ni and Co elements. Figure 3b–d show the XPS spectra in the C 1s, Ni 2p, and Co 2p regions. As shown in Figure 3b, the C 1s spectrum presents three

peaks located at 284.58 eV, 285.88 eV, and 287.78 eV, corresponding to the binding energy (BE) of C-C, C-O, and O-C=O, respectively [39]. Figure 3c shows that for Ni 2p, the two peaks of 855.68 eV and 873.18 eV were consistent with the BEs of Ni 2p_{3/2} and Co 2p_{1/2}, respectively, confirming the presence of the Ni element in the form of metallic Ni. The BEs at 861.18 eV and 879.68 eV with two satellites also corresponded to metallic Ni [40,41]. The high-resolution Co 2p spectrum was fitted into four peaks (Figure 3d). The doublet peaks at 776.28 eV and 789.98 eV were ascribed to the Co⁰ 2p_{3/2} and Co⁰ 2p_{1/2}, while the doublet peaks at 781.28 eV and 797.68 eV were attributed to the Co²⁺ 2p_{3/2} and Co²⁺ 2p_{1/2}, respectively. The BEs at 785.58 eV and 803.78 eV with two satellite peaks indicated the existence of Co [41–43]. When the peaks of the BEs were combined with EDS (Figure 1d–f), the ratio of Ni and Co was about 50:50 as a whole, suggesting that the loading of metallic NiCo was successful.

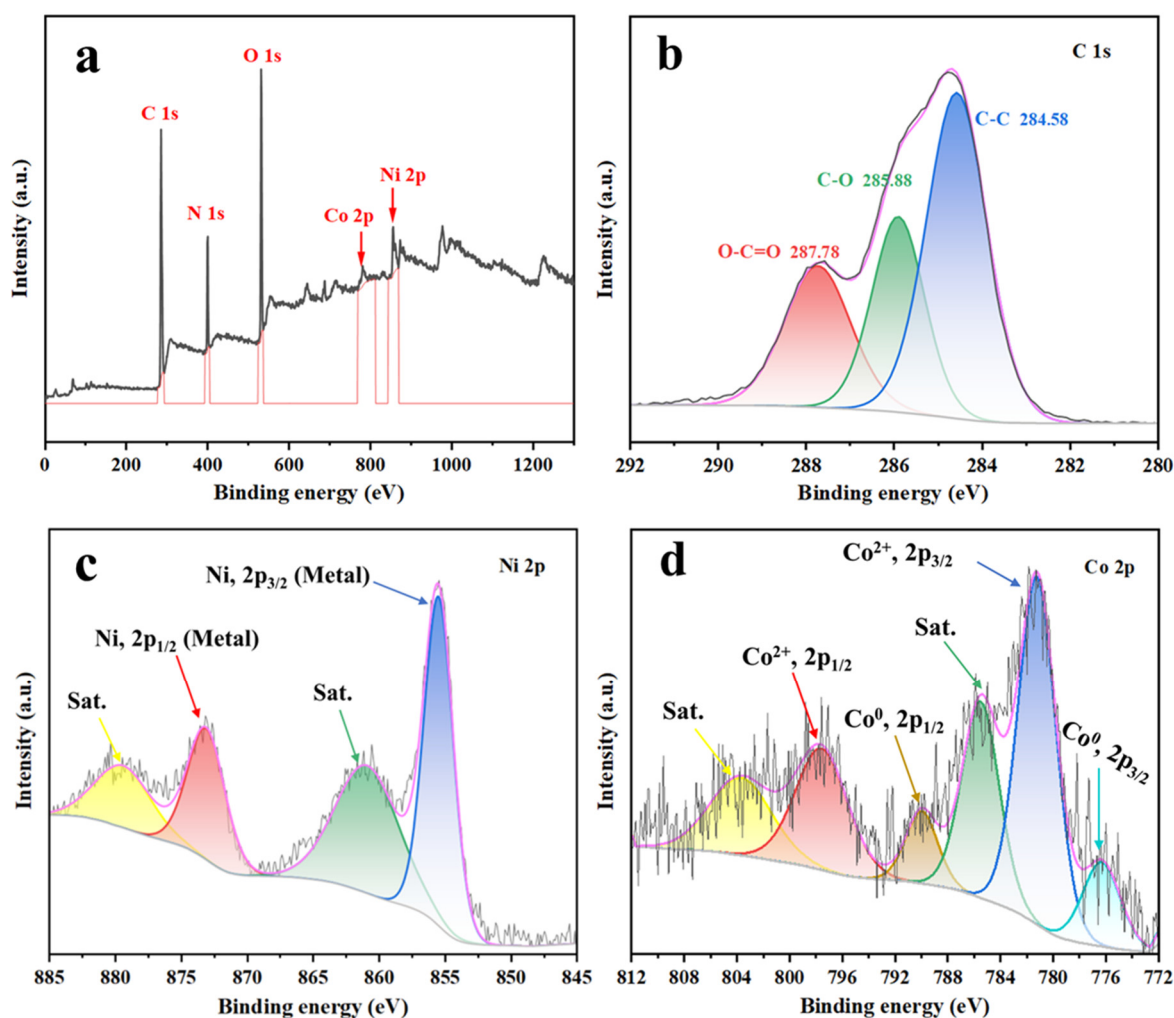


Figure 3. XPS survey for Ni₂Co₂/Silk-PVDF in the (a) XPS survey, (b) C 1s, (c) Ni 2p, and (d) Co 2p.

2.2. Electrochemical Properties of the Ni_xCo_x/Silk-PVDF Electrodes

The silk self-supporting electrode was used as the working electrode. The activity of HER was measured with the traditional three-electrode system structure, and a Pt electrode was used as the counter electrode. Their catalytic activities in a 1 M KOH solution were determined by using linear sweep voltammetry (LSV) [44]. Figure 4a shows the LSV curves of different catalysts in the potential range of -0.4 V– 0 V (vs. RHE) with a scanning rate of 5 mV s⁻¹. The overpotentials of the Ni₁Co₁/Silk-PVDF and the Ni₂Co₂/Silk-PVDF electrodes reached 179.4 mV and 161.7 mV at a current density of 100 mA cm⁻², respectively. Meanwhile, the electrodes loaded with the single metals

Ni and Co showed insignificant catalytic activity, and the current density did not reach 100 mA cm^{-2} . In summary, the $\text{Ni}_2\text{Co}_2/\text{Silk-PVDF}$ electrocatalysts showed the best HER performance among all electrocatalysts synthesized in this study.

Figure 4b shows the Tafel slopes. The Tafel slope is determined according to the η (overpotential) and j (current density) values in the LSV curve, which reflect the change in the steady-state current under different overpotentials. The linear portion of the Tafel plot corresponds to the equation $\eta = a + b \times \log j$, where b is the Tafel slope and a is the constant of the material [20,45]. Tafel data can be verified by LSV and converted from LSV's ordinate to Tafel's abscissa through $\log | \text{current density} |$ calculation. The smaller the Tafel is, the higher the current density that can be achieved with a lower overpotential; thus, the Tafel slope is related to the mechanism of HER [46]. The Tafel slopes of the Co/Silk-PVDF, Ni/Silk-PVDF, $\text{Ni}_1\text{Co}_1/\text{Silk-PVDF}$, and $\text{Ni}_2\text{Co}_2/\text{Silk-PVDF}$ electrodes were $219.67 \text{ mV dec}^{-1}$, $121.14 \text{ mV dec}^{-1}$, $93.65 \text{ mV dec}^{-1}$, and $67.46 \text{ mV dec}^{-1}$, respectively, indicating that the $\text{Ni}_2\text{Co}_2/\text{Silk-PVDF}$ bimetal exhibited higher catalytic activity than the other three HER catalysts. Consequently, all the samples loaded with the same quality metal were tested to confirm that the best catalytic performance was provided by the $\text{Ni}_2\text{Co}_2/\text{Silk-PVDF}$ electrode. The Tafel slope of the $\text{Ni}_2\text{Co}_2/\text{Silk-PVDF}$ electrode ($67.46 \text{ mV dec}^{-1}$) was slightly larger than that of the commercial Pt/C electrode (42.6 mV dec^{-1}) [47]; however, it had better performance than most NiCo catalysts reported to date (Table 1) [20,48,49].

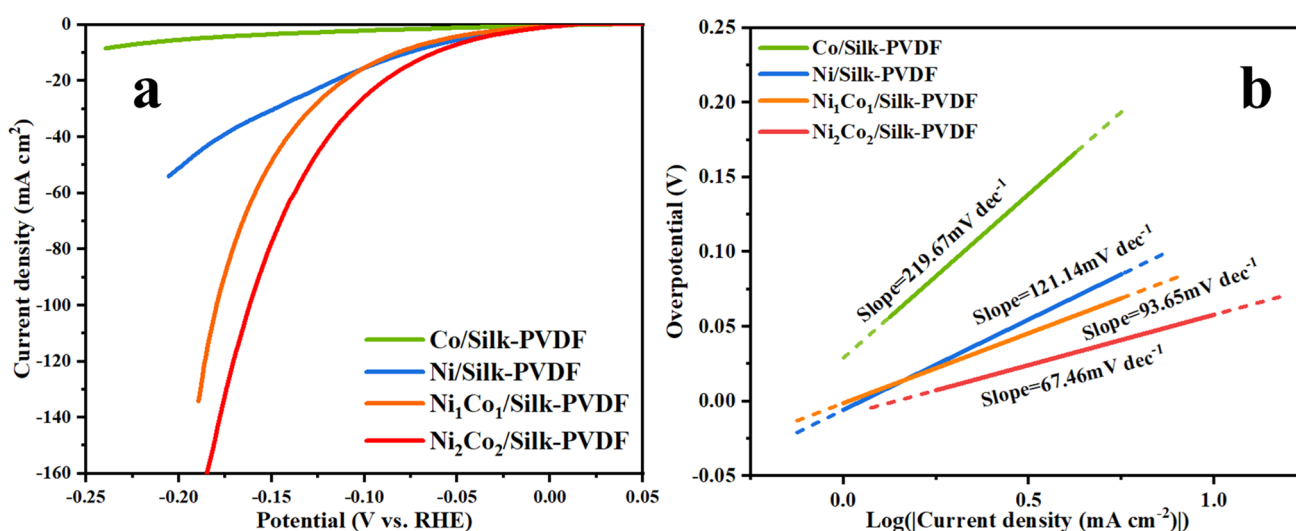


Figure 4. LSV curves (a) and Tafel plots (b) for the $\text{Ni}_x\text{Co}_x/\text{Silk-PVDF}$ electrodes.

Table 1. The comparative set up showing HER activities of the present work with reported data.

Catalysts	Electrolyte	Overpotential/ (mV)	Tafel Slope (mV dec^{-1})	J (mA cm^{-2})	Ref.
NiFeCo	1.0 M KOH	64	64	10	[50]
$\text{Co}_{0.5}\text{Zn}_{0.5}\text{MoO}_4$	1.0 M KOH	201	162.7	10	[51]
$\text{Ti}_3\text{C}_2\text{Tx@ZIF-8}$	1.0 M KOH	107	77	20	[52]
NiSSe	1.0 M KOH	154	125	10	[53]
Fe-NiS ₂	0.5 M H ₂ SO ₄	198	42	10	[54]
NiTe ₂	0.5 M H ₂ SO ₄	560	44	10	[55]
$\text{Ni}_{95}\text{Fe}_5/\text{CP}$	1.0 M KOH	130	95.4	20	[20]
NiCl ₂	1.0 M KOH	176	41	10	[56]
10% F/BCN	0.5 M H ₂ SO ₄	222	87	10	[57]
$\text{Ni}_2\text{Co}_2/\text{Silk-PVDF}$	1.0 M KOH	89.4	67.46	20	This work

Furthermore, electrochemical impedance spectroscopy (EIS) was used to explore the mechanical process kinetics of HER at the electrode interface. The Randles equivalent circuit is used in EIS analysis and includes R_s (solution resistance), R_{ct} (charge transfer resistance), and C_{dl} (electrochemical double-layer capacitance) [58,59]. Usually, the semicircle radius

of impedance in the low-frequency region of the EIS diagram is directly related to the charge transfer resistance. Therefore, a smaller semicircle induces better electrode electrical conductivity. The R_{ct} values of the Co/Silk-PVDF, Ni/Silk-PVDF, Ni₁Co₁/Silk-PVDF, and Ni₂Co₂/Silk-PVDF electrodes were 8.61 Ω , 8.032 Ω , 4.629 Ω , and 3.847 Ω , respectively. Obviously, the impedance semicircle radius of the Ni₂Co₂/Silk-PVDF electrode catalyst was smaller than that of the other three electrodes. The recorded EIS Nyquist plot was perfectly fitted with the proposed equivalent circuit, as shown in the inset of Figure 5a. In particular, the Ni₂Co₂/Silk-PVDF electrode showed the lowest resistance, which meant that the dynamics of the hydrogen evolution reaction of the Ni₂Co₂/Silk-PVDF were faster; thus, it had the best charge transfer efficiency.

The double-layer capacitance (C_{dl}) is shown in Figure 5b,c. A double-layer capacitor was used to estimate the electrochemically active surface area (ECSA) [60], as shown in Figure 5b, at a scan rate of 120 mV s^{-1} and a voltage window of 0.18 V–0.28 V. The value of the ECSA directly affects the performance of HER. The width of the electrode CV curve increased sharply with the addition of the NiCo bimetal. In addition, the Ni₂Co₂/Silk-PVDF electrode displayed symmetrical CV curves with no obvious pseudocapacitive behavior at a voltage window of 0.18 V–0.28 V and scan rates of 20 mV s^{-1} , 40 mV s^{-1} , 60 mV s^{-1} , 80 mV s^{-1} , and 120 mV s^{-1} (Figure 5c) [61], indicating that this electrode had a low charge-transfer resistance. The C_{dl} value trend lines were calculated from the slopes of the CV curve, and the value of the Ni₂Co₂/Silk-PVDF electrode was 133.04 mF cm^{-2} (Figure 5d) [62]. Obviously, the Ni₂Co₂/Silk-PVDF electrode exhibited the highest C_{dl} value. Thus, the Ni₂Co₂/Silk-PVDF electrode was expected to exhibit excellent electrocatalytic activity because of its high electrical capacity.

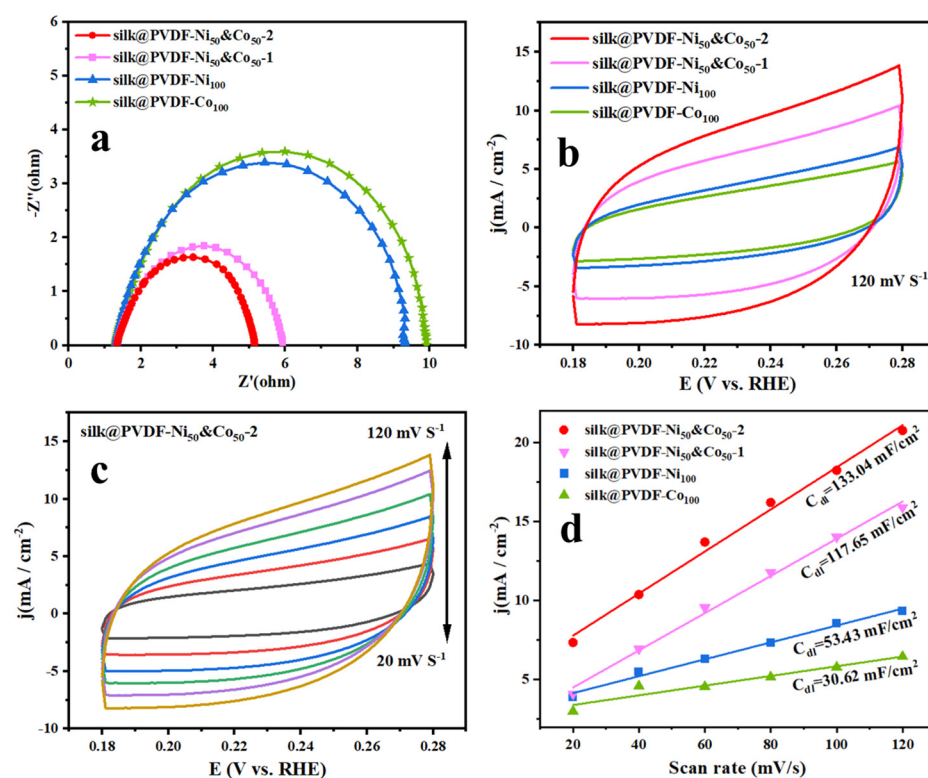


Figure 5. EIS (a), ECSA (b), and electrochemical double-layer capacitance (C_{dl}) (c) of the Ni_xCo_x/Silk-PVDF electrodes. (d) Nyquist plots for the Ni_xCo_x/Silk-PVDF electrodes.

Long-term stability is a very important indicator for commercial use. As shown in Figure 6a, we observed the change in current density at a constant potential difference of -0.1 V. The current density of the Ni₂Co₂/Silk-PVDF electrode decreased very little within 90,000 s, whereas that of the Ni₂Co₂/Silk electrode rapidly changed in a relatively short period of time. Figure 6b, 6c show the morphology of the Ni₂Co₂/Silk electrode and the

$\text{Ni}_2\text{Co}_2/\text{Silk-PVDF}$ electrode during electrochemical stability tests for 7000 s and 90,000 s, respectively. It was obvious that the PVDF still retained the original electrode shape after the electrode was tested for 90,000 s, which proves that PVDF can improve the durability of silk electrodes.

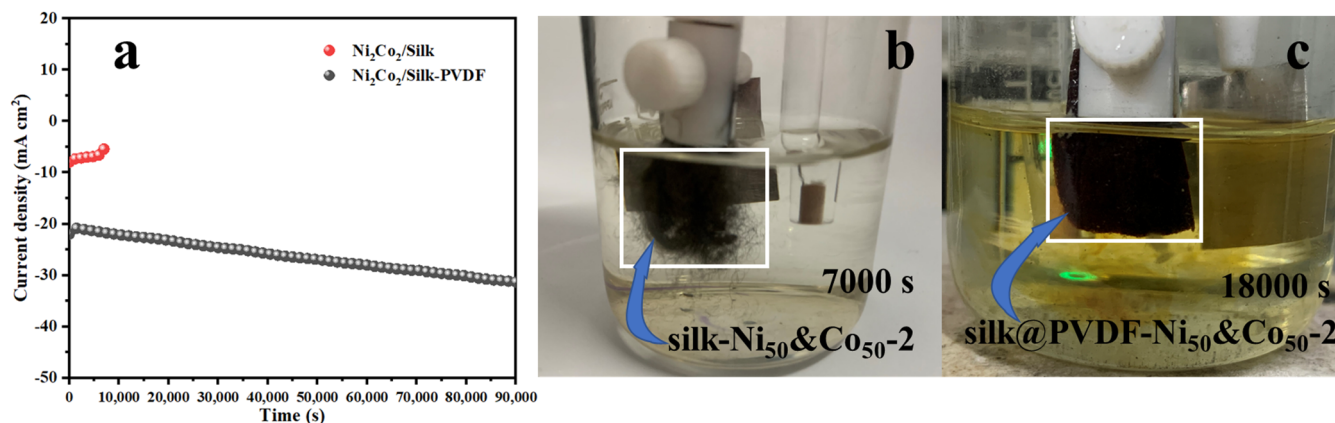


Figure 6. Time-dependent current density changes for various electrodes under a constant potential of -0.1 V (vs RHE) (a), the morphology of the $\text{Ni}_2\text{Co}_2/\text{Silk}$ electrode after testing (b), and the morphology of the $\text{Ni}_2\text{Co}_2/\text{Silk-PVDF}$ electrode after testing (c).

3. Experimental Section

3.1. Reagents and Materials

Nickel nitrate hexahydrate ($\text{Ni}(\text{NO}_3)_2 \cdot 6\text{H}_2\text{O}$, GR, 99%, CAS: 13478-00-7) was commercially available from Sinopharm Chemical Reagent Co., Ltd. (Shanghai, China). Cobaltous nitrate hexahydrate ($\text{Co}(\text{NO}_3)_2 \cdot 6\text{H}_2\text{O}$, AR, 99%, CAS: 10026-22-9) was purchased from the Chengdu Kelong Chemical Reagent Company (Chengdu, China). N,N-dimethylformamide (DMF, GC, 99.9%, CAS: 68-12-2), 2-methylimidazole (HMIIm, 98%, CAS: 693-98-1), polyvinylidene difluoride (PVDF, average Mw: 2.75×10^5 , average Mn: 1.07×10^5 , CAS: 24937-79-9), and polyvinyl pyrrolidone (PVP, average Mw: 5.5×10^4 , CAS: 9003-39-8) were provided by Shanghai Civi Chemical Technology Co., Ltd. (Shanghai, China). Methanol (AR, 99.5%, CAS: 67-56-1) and potassium hydroxide (KOH, AR, 99%, CAS: 1310-58-3) were purchased from Shanghai Aladdin Biochemical Technology Co., Ltd. (Shanghai, China).

3.2. Preparation of Silk-PVDF

Waste silk was collected from a recycling station. The waste silk was cut into 1×2 cm pieces [63,64]. A total of 5 g of PVDF powder, 0.33 g of PVP, and 5 g of HMIIm were added to 28 mL of DMF solvent and dissolved via magnetic stirring in an oil bath at 60°C for 12 h to obtain a uniform brown, transparent solution. The obtained solution was then scraped evenly on the silk surface before being transferred to an air oven at 60°C for 8 h to dry and obtain the Silk-PVDF sample.

3.3. Electrode Preparation

Briefly, the dried Silk-PVDF was laid at the bottom of a hydrothermal kettle; then, $\text{Ni}(\text{NO}_3)_2 \cdot 6\text{H}_2\text{O}$ and $\text{Co}(\text{NO}_3)_2 \cdot 6\text{H}_2\text{O}$ were added to a beaker containing DMF and HMIIm, respectively. At this time, the molar mass ratios of Ni:Co were adjusted to 0:100, 100:0, and 50:50, corresponding to samples Co/Silk-PVDF, Ni/Silk-PVDF, and $\text{Ni}_1\text{Co}_1/\text{Silk-PVDF}$. A subsequent separate weighing of Ni and Co with a molar mass ratio of 50:50 was half that of $\text{Ni}_1\text{Co}_1/\text{Silk-PVDF}$ as the first hydrothermal condition of $\text{Ni}_2\text{Co}_2/\text{Silk-PVDF}$. The samples were thoroughly stirred and added to the hydrothermal kettle. The hydrothermal kettle was then transferred to the air oven, where the temperature was raised to 140°C for 2 h, and the reaction was allowed to progress for 48 h. After the reaction, the filter paper at the bottom of the kettle was removed, cleaned with DMF and methanol, and dried in an air oven at 60°C for 8 h. Finally, according to the above $\text{Ni}_2\text{Co}_2/\text{Silk-PVDF}$ experimental

conditions, the secondary hydrothermal process was carried out. There are two schemes for the synthesis of bimetallic NiCo, 'Ni₁Co₁/Silk-PVDF' and 'Ni₂Co₂/Silk-PVDF'. For example, the Ni₁Co₁/Silk-PVDF uses 0.2 g Ni(NO₃)₂·6H₂O and 0.2 g Co(NO₃)₂·6H₂O for one solvothermal synthesis. The Ni₂Co₂/Silk-PVDF uses 0.1 g Ni(NO₃)₂·6H₂O and 0.1 g Co(NO₃)₂·6H₂O for first solvothermal synthesis. After the completion of first solvothermal synthesis, 0.1 g Ni(NO₃)₂·6H₂O and 0.1 g Co(NO₃)₂·6H₂O were used for second solvothermal synthesis. It means that the total quality of Ni(NO₃)₂·6H₂O and Co(NO₃)₂·6H₂O was 0.4 g for Ni₁Co₁/Silk-PVDF and Ni₂Co₂/Silk-PVDF. The Ni₂Co₂/Silk-PVDF electrode was obtained after rinsing and drying for further analysis (Figure 1).

3.4. Physicochemical Characterization of Electrocatalysts

The Ni_xCo_x/Silk-PVDF electrodes were analyzed via X-ray diffraction (XRD, PW3040/60, Philips, Tokyo, Japan). The XRD patterns of a catalyst were recorded over the scanning range of 2θ (5° to 90°) with Cu Kα radiation, the target voltage was 40 kV and the current was 30 mA. By comparing the diffraction peaks of the measured XRD spectrum with a standard, the composition and crystal structure of the sample can be determined. The morphology, size, and distribution of the Ni₂Co₂/Silk-PVDF electrodes was observed through the use of scanning electron microscopy (SEM, Sigma 300, Zeiss, Oberkochen, Germany) and energy-dispersive X-ray spectroscopy (EDS). The SEM tests were performed with a 10 kV electron beam. The SEM images were taken with an InLens at magnifications ranging from 20,000× to 50,000×. X-ray photoelectron spectroscopy (XPS, Thermo Fisher Nexsa, Waltham, MA, USA) was used to determine the chemical composition and valence of the elements in the samples. All XPS spectra were corrected to the binding energy (BE) of C 1 s = 284.58 eV. The ultrastructure of the samples was observed using an ultra-high-resolution transmission electron microscope (TEM, JEM 2100, JEOL, Tokyo, Japan).

3.5. Evaluation of Electrochemical Properties

All electrochemical tests were conducted at an electrochemical workstation (CHI760E, Shanghai, China). The cyclic voltammetry (CV), electrochemical impedance spectrum (EIS), linear sweep voltammetry (LSV), and long-term stability were tested using a standard three-electrode system (Ni_xCo_x/Silk-PVDF (working electrode area: 1 × 1 cm²), a Pt sheet, and a saturated calomel electrode (RHE, $E_{\text{RHE}} = E_{\text{Hg}/\text{Hg}_2\text{Cl}_2} + 0.0592 \times \text{pH} + 0.24 \text{ V}$) reacted in 1 M KOH electrolyte [65]. The electrochemical double-layer capacitance (C_{dl}) of the Ni_xCo_x/Silk-PVDF electrodes was obtained via CV measurements at scan rates of 20, 40, 60, 80, 100, and 120 mV s⁻¹ over the non-Faradaic region. The electrode polarization curves were recorded by performing LSV measurements. The Tafel slopes of electrodes were calculated from the LSV curves. A frequency ranging from 0.1 Hz to 100 kHz with a scan rate of 5 mV s⁻¹ at open circuit potential was used to test EIS. Long-term stability under the same conditions was set at 90,000 s (over 24 h). This was used to assess the durability and stability of the electrode.

4. Conclusions

In this study, Ni_xCo_x/Silk-PVDF bimetal catalysts were designed via PVDF wrapping and hydrothermal synthesis. Silk, as a self-supporting electrode, was used as the working electrode. By varying the Ni and Co ratio, four different samples were prepared: Co/Silk-PVDF, Ni/Silk-PVDF, Ni₁Co₁/Silk-PVDF, and Ni₂Co₂/Silk-PVDF. The results of XRD, XPS, and TEM revealed the existence of the Ni and Co elements. The XRD diffraction peaks of bimetallic electrodes were significantly stronger than those of monometallic electrodes. In particular, Ni₂Co₂/Silk-PVDF had the highest intensity of diffraction peaks. The XPS revealed the presence of elements and the intensity of their binding energy. The TEM images showed that the lattice fringes of the metal Co and Ni. The EDS images showed that the Ni and Co elements were evenly distributed. The ratio of Ni and Co was in line with our expectations. As shown by electrochemistry, when the current density was 10 mA cm⁻², the overpotential of the Ni₂Co₂/Silk-PVDF was 89.4 mV. Furthermore, the

Tafel slope of the Ni₂Co₂/Silk-PVDF was just 67.46 mV dec⁻¹. The Nyquist plots showed its *R*_{ct} value was 3.847 Ω. At a scan rate of 120 mV s⁻¹, the electrode showed the widest CV curves, indicating that its ECSA was the largest. Meanwhile, the electrode's C_{dl} value was 133.04 mF cm². After stability and long-term testing, there was a significant difference in the morphology of silk before and after wrapping with PVDF. Therefore, the proposed route can provide a reference for the preparation of electrochemical catalysts in the field of green, renewable biomass.

Author Contributions: Conceptualization, H.W. and C.Z.; methodology, H.W.; software, H.W.; validation, Y.W., Z.L. and L.S.; formal analysis, H.W.; investigation, H.W.; data curation, H.W.; writing—original draft preparation, H.W.; writing—review and editing, H.W.; visualization, H.W.; supervision, C.Z.; project administration, C.Z.; funding acquisition, C.Z. All authors have read and agreed to the published version of the manuscript.

Funding: This research was funded by [Postgraduate Research & Practice Innovation Program of Jiangsu Province] grant number [SJCX22_1456] and [SJCX22_1459], [the National Natural Science Foundation of China] grant number [31800495], [Natural Science Foundation of Jiangsu Province] grant number [BK20181040].

Data Availability Statement: Not applicable.

Conflicts of Interest: The authors declare no conflict of interest.

References

1. Wijayanta, A.T.; Oda, T.; Purnomo, C.W.; Kashiwagi, T.; Aziz, M. Liquid hydrogen, methylcyclohexane, and ammonia as potential hydrogen storage: Comparison review. *Int. J. Hydrogen Energy* **2019**, *44*, 15026–15044. [[CrossRef](#)]
2. Brewer, G.D. Aviation usage of liquid hydrogen fuel—Prospects and problems. *Int. J. Hydrogen Energy* **1976**, *1*, 65–88. [[CrossRef](#)]
3. Morales-Guio, C.G.; Liardet, L.; Mayer, M.T.; Tilley, S.D.; Grätzel, M.; Hu, X. Photoelectrochemical Hydrogen Production in Alkaline Solutions Using Cu₂O Coated with Earth-Abundant Hydrogen Evolution Catalysts. *Angew. Chem. Int. Ed.* **2015**, *54*, 664–667. [[CrossRef](#)]
4. Kim, S.-j.; Jung, H.; Lee, C.; Kim, M.H.; Lee, Y. Comparative Study on Hydrogen Evolution Reaction Activity of Electrospun Nanofibers with Diverse Metallic Ir and IrO₂ Composition Ratios. *ACS Sustain. Chem. Eng.* **2019**, *7*, 8613–8620. [[CrossRef](#)]
5. Liu, S.-S.; Ma, L.-J.; Li, J.-S. Dual-metal-organic-framework derived CoP/MoP hybrid as an efficient electrocatalyst for acidic and alkaline hydrogen evolution reaction. *J. Colloid Interface Sci.* **2023**, *631*, 147–153. [[CrossRef](#)]
6. Zhao, W.; Wang, S.; Feng, C.; Wu, H.; Zhang, L.; Zhang, J. Novel Cobalt-Doped Ni_{0.85}Se Chalcogenides (Co_xNi_{0.85-x}Se) as High Active and Stable Electrocatalysts for Hydrogen Evolution Reaction in Electrolysis Water Splitting. *ACS Appl. Mater. Interfaces* **2018**, *10*, 40491–40499. [[CrossRef](#)] [[PubMed](#)]
7. Kim, C.; Lee, S.; Kim, S.H.; Park, J.; Kim, S.; Kwon, S.-H.; Bae, J.-S.; Park, Y.S.; Kim, Y. Cobalt–Iron–Phosphate Hydrogen Evolution Reaction Electrocatalyst for Solar-Driven Alkaline Seawater Electrolyzer. *Nanomaterials* **2021**, *11*, 2989. [[CrossRef](#)] [[PubMed](#)]
8. Dai, J.; Zhu, Y.; Tahini, H.A.; Lin, Q.; Chen, Y.; Guan, D.; Zhou, C.; Hu, Z.; Lin, H.-J.; Chan, T.-S.; et al. Single-phase perovskite oxide with super-exchange induced atomic-scale synergistic active centers enables ultrafast hydrogen evolution. *Nat. Commun.* **2020**, *11*, 5657. [[CrossRef](#)] [[PubMed](#)]
9. Wang, C.; Li, C.; Liu, J.; Guo, C. Engineering transition metal-based nanomaterials for high-performance electrocatalysis. *Mater. Rep. Energy* **2021**, *1*, 100006. [[CrossRef](#)]
10. Guan, D.; Zhou, J.; Huang, Y.-C.; Dong, C.-L.; Wang, J.-Q.; Zhou, W.; Shao, Z. Screening highly active perovskites for hydrogen-evolving reaction via unifying ionic electronegativity descriptor. *Nat. Commun.* **2019**, *10*, 3755. [[CrossRef](#)]
11. Abdelgawad, A.; Salah, B.; Lu, Q.; Abdullah, A.M.; Chitt, M.; Ghanem, A.; Al-Hajri, R.S.; Eid, K. Template-free synthesis of M/g-C₃N₄ (M = Cu, Mn, and Fe) porous one-dimensional nanostructures for green hydrogen production. *J. Electroanal. Chem.* **2023**, *938*, 117426. [[CrossRef](#)]
12. Atchudan, R.; Perumal, S.; Jebakumar Immanuel Edison, T.N.; Sundramoorthy, A.K.; Karthik, N.; Sangaraju, S.; Choi, S.T.; Lee, Y.R. Biowaste-Derived Heteroatom-Doped Porous Carbon as a Sustainable Electrocatalyst for Hydrogen Evolution Reaction. *Catalysts* **2023**, *13*, 542. [[CrossRef](#)]
13. Irvani, S.; Varma, R.S. Green synthesis, biomedical and biotechnological applications of carbon and graphene quantum dots. A review. *Environ. Chem. Lett.* **2020**, *18*, 703–727. [[CrossRef](#)] [[PubMed](#)]
14. Murugesan, C.; Senthilkumar, B.; Barpanda, P. Biowaste-Derived Highly Porous N-Doped Carbon as a Low-Cost Bifunctional Electrocatalyst for Hybrid Sodium–Air Batteries. *ACS Sustain. Chem. Eng.* **2022**, *10*, 9077–9086. [[CrossRef](#)]
15. Reier, T.; Oezaslan, M.; Strasser, P. Electrocatalytic Oxygen Evolution Reaction (OER) on Ru, Ir, and Pt Catalysts: A Comparative Study of Nanoparticles and Bulk Materials. *ACS Catal.* **2012**, *2*, 1765–1772. [[CrossRef](#)]
16. Deng, X.; Mi, Y.; Liu, Y.; Sun, Y.; Cheng, Y.; Wang, W. Co, N co-doped carbon nanosheets coupled with NiCo₂O₄ as an efficient bifunctional oxygen catalyst for Zn-air batteries. *Int. J. Hydrogen Energy* **2023**, *48*, 13452–13459. [[CrossRef](#)]

17. Wang, C.; Du, X.; Zhang, X. Controlled synthesis of W-Co₃S₄@Co₃O₄ as an environmentally friendly and low cost electrocatalyst for overall water splitting. *Int. J. Hydrogen Energy* **2023**, *48*, 12739–12752. [[CrossRef](#)]
18. Liu, Q.; Wang, Y.; Lu, X. Construction of NiFe-Layered Double Hydroxides Arrays as Robust Electrocatalyst for Oxygen Evolution Reaction. *Catalysts* **2023**, *13*, 586. [[CrossRef](#)]
19. Xu, X.; Shao, Z.; Jiang, S.P. High-Entropy Materials for Water Electrolysis. *Energy Technol.* **2022**, *10*, 2200573. [[CrossRef](#)]
20. Lee, J.; Son, N.; Shin, J.; Pandey, S.; Woo Joo, S.; Kang, M. Highly efficient hydrogen evolution reaction performance and long-term stability of spherical Ni_{100-x}Fe_x alloy grown directly on a carbon paper electrode. *J. Alloys Compd.* **2021**, *869*, 159265. [[CrossRef](#)]
21. Zou, X.; Zhang, Y. Noble metal-free hydrogen evolution catalysts for water splitting. *Chem. Soc. Rev.* **2015**, *44*, 5148–5180. [[CrossRef](#)] [[PubMed](#)]
22. Shetty, S.; Mohamed Jaffer Sadiq, M.; Bhat, D.K.; Hegde, A.C. Electrodeposition and characterization of Ni-Mo alloy as an electrocatalyst for alkaline water electrolysis. *J. Electroanal. Chem.* **2017**, *796*, 57–65. [[CrossRef](#)]
23. Li, K.; Li, Y.; Wang, Y.; Ge, J.; Liu, C.; Xing, W. Enhanced electrocatalytic performance for the hydrogen evolution reaction through surface enrichment of platinum nanoclusters alloying with ruthenium in situ embedded in carbon. *Energy Environ. Sci.* **2018**, *11*, 1232–1239. [[CrossRef](#)]
24. Popov, A.A.; Afonnikova, S.D.; Varygin, A.D.; Bauman, Y.I.; Trenikhin, M.V.; Plyusnin, P.E.; Shubin, Y.V.; Vedyagin, A.A.; Mishakov, I.V. Pt_{1-x}Ni_x Alloy Nanoparticles Embedded in Self-Grown Carbon Nanofibers: Synthesis, Properties and Catalytic Activity in HER. *Catalysts* **2023**, *13*, 599. [[CrossRef](#)]
25. Nguyen, V.-T.; Lee, G.-J.; Ngo, Q.-T.; Omelianovych, O.; Nguyen, N.-A.; Trinh, V.-H.; Choi, H.-S.; Mnoyan, A.; Lee, K.; Larina, L.L.; et al. Robust carbon-encapsulated Ni nanoparticles as high-performance electrocatalysts for the hydrogen evolution reaction in highly acidic media. *Electrochim. Acta* **2021**, *398*, 139332. [[CrossRef](#)]
26. Xu, Y.; Wang, R.; Zheng, Y.; Zhang, L.; Jiao, T.; Peng, Q.; Liu, Z. Facile preparation of self-assembled Ni/Co phosphates composite spheres with highly efficient HER electrocatalytic performances. *Appl. Surf. Sci.* **2020**, *509*, 145383. [[CrossRef](#)]
27. Hu, E.; Feng, Y.; Nai, J.; Zhao, D.; Hu, Y.; Lou, X.W. Construction of hierarchical Ni-Co-P hollow nanobricks with oriented nanosheets for efficient overall water splitting. *Energy Environ. Sci.* **2018**, *11*, 872–880. [[CrossRef](#)]
28. Gorospe, A.E.G.B.; Balela, M.D.L. Ni-Co nanocomposites deposited on carbon fiber paper as an electrocatalyst towards hydrogen evolution reaction. *Mater. Today Proc.* **2020**, *22*, 255–261. [[CrossRef](#)]
29. Lupi, C.; Dell’Era, A.; Pasquali, M. Nickel-cobalt electrodeposited alloys for hydrogen evolution in alkaline media. *Int. J. Hydrogen Energy* **2009**, *34*, 2101–2106. [[CrossRef](#)]
30. Nakamura, A.; Koguchi, M.; Masaaki Futamoto, M.F. Microstructures of Co/Cr Bilayer Films Epitaxially Grown on MgO Single-Crystal Substrates. *Jpn. J. Appl. Phys.* **1995**, *34*, 2307. [[CrossRef](#)]
31. Chun, C.M.; Mumford, J.D.; Ramanarayanan, T.A. Carbon-Induced Corrosion of Nickel Anode. *J. Electrochem. Soc.* **2000**, *147*, 3680. [[CrossRef](#)]
32. Zhengshi, Z.; Zhaozhao, D.; Jiwei, H.; Jianzhong, Q.; Yixin, S.; Feng, Z.; Baoqi, Z. Green process to prepare water-insoluble silk scaffolds with silk I structure. *Int. J. Biol. Macromol.* **2018**, *117*, 144–151. [[CrossRef](#)] [[PubMed](#)]
33. Drummy, L.F.; Phillips, D.M.; Stone, M.O.; Farmer, B.L.; Naik, R.R. Thermally Induced α -Helix to β -Sheet Transition in Regenerated Silk Fibers and Films. *Biomacromolecules* **2005**, *6*, 3328–3333. [[CrossRef](#)] [[PubMed](#)]
34. Yu, L.-M.; Liu, T.; Ma, Y.-L.; Zhang, F.; Huang, Y.-C.; Fan, Z.-H. Fabrication of Silk-Hyaluronan Composite as a Potential Scaffold for Tissue Repair. *Front. Bioeng. Biotechnol.* **2020**, *8*, 578988. [[CrossRef](#)]
35. Prasad, P.D.; Hemalatha, J. Multifunctional films of poly(vinylidene fluoride)/ZnFe₂O₄ nanofibers for nanogenerator applications. *J. Alloys Compd.* **2021**, *854*, 157189. [[CrossRef](#)]
36. Wang, H.; Kou, X.; Zhang, J.; Li, J. Large scale synthesis and characterization of Ni nanoparticles by solution reduction method. *Bull. Mater. Sci.* **2008**, *31*, 97–100. [[CrossRef](#)]
37. Przydacz, M.; Jędrzejczyk, M.; Rogowski, J.; Szyrkowska-Jóźwik, M.; Ruppert, A.M. Highly Efficient Production of DMF from Biomass-Derived HMF on Recyclable Ni-Fe/TiO₂ Catalysts. *Energies* **2020**, *13*, 4660. [[CrossRef](#)]
38. Huang, W.; Zuo, Z.; Han, P.; Li, Z.; Zhao, T. XPS and XRD investigation of Co/Pd/TiO₂ catalysts by different preparation methods. *J. Electron Spectrosc. Relat. Phenom.* **2009**, *173*, 88–95. [[CrossRef](#)]
39. Heeg, J.; Schubert, U.; Küchenmeister, F. Surface Chemistry of Planarized SiLK-Films Studied by XPS. *Microchim. Acta* **2000**, *133*, 113–117. [[CrossRef](#)]
40. Mingli, F.; Xue, L.; Dandan, W.; Yinling, W.; Maoguo, L. Fabrication of Te@NiTe₂/NiS heterostructures for electrocatalytic hydrogen evolution reaction. *Electrochim. Acta* **2019**, *328*, 135075. [[CrossRef](#)]
41. Paudel, D.R.; Pan, U.N.; Ghising, R.B.; Dhakal, P.P.; Dinh, V.A.; Wang, H.; Kim, N.H.; Lee, J.H. Interface modulation induced by the 1T Co-WS₂ shell nanosheet layer at the metallic NiTe₂/Ni core-nanoskeleton: Glib electrode-kinetics for HER, OER, and ORR. *Nano Energy* **2022**, *102*, 107712. [[CrossRef](#)]
42. Xiong, X.; You, C.; Liu, Z.; Asiri, A.M.; Sun, X. Co-Doped CuO Nanoarray: An Efficient Oxygen Evolution Reaction Electrocatalyst with Enhanced Activity. *ACS Sustain. Chem. Eng.* **2018**, *6*, 2883–2887. [[CrossRef](#)]
43. Zhu, H.; Zhu, Z.; Hao, J.; Sun, S.; Lu, S.; Wang, C.; Ma, P.; Dong, W.; Du, M. High-entropy alloy stabilized active Ir for highly efficient acidic oxygen evolution. *Chem. Eng. J.* **2022**, *431*, 133251. [[CrossRef](#)]
44. Fu, Q.; Han, J.; Wang, X.; Xu, P.; Yao, T.; Zhong, J.; Zhong, W.; Liu, S.; Gao, T.; Zhang, Z.; et al. 2D Transition Metal Dichalcogenides: Design, Modulation, and Challenges in Electrocatalysis. *Adv. Mater.* **2021**, *33*, 1907818. [[CrossRef](#)] [[PubMed](#)]

45. Guo, W.; Le, Q.V.; Do, H.H.; Hasani, A.; Tekalgne, M.; Bae, S.-R.; Lee, T.H.; Jang, H.W.; Ahn, S.H.; Kim, S.Y. Ni₃Se₄@MoSe₂ Composites for Hydrogen Evolution Reaction. *Appl. Sci.* **2019**, *9*, 5035. [[CrossRef](#)]
46. Zeng, M.; Li, Y. Recent advances in heterogeneous electrocatalysts for the hydrogen evolution reaction. *J. Mater. Chem. A* **2015**, *3*, 14942–14962. [[CrossRef](#)]
47. Wu, C.; Liu, D.; Li, H.; Li, J. Molybdenum Carbide-Decorated Metallic Cobalt@Nitrogen-Doped Carbon Polyhedrons for Enhanced Electrocatalytic Hydrogen Evolution. *Small* **2018**, *14*, 1704227. [[CrossRef](#)]
48. Skibińska, K.; Wojtaszek, K.; Krause, L.; Kula, A.; Yang, X.; Marzec, M.M.; Wojnicki, M.; Żabiński, P. Tuning up catalytical properties of electrochemically prepared nanoconical Co-Ni deposit for HER and OER. *Appl. Surf. Sci.* **2023**, *607*, 155004. [[CrossRef](#)]
49. Qian, Y.; Hu, M.; Li, L.; Liu, X.; Cao, S.; Guo, C. Graphene oxide decorated nickel-cobalt nanosheet structures based on carbonized wood for electrocatalytic hydrogen evolution. *Int. J. Hydrogen Energy* **2023**, *48*, 13543–13554. [[CrossRef](#)]
50. Babar, P.; Lokhande, A.; Karade, V.; Pawar, B.; Gang, M.G.; Pawar, S.; Kim, J.H. Bifunctional 2D Electrocatalysts of Transition Metal Hydroxide Nanosheet Arrays for Water Splitting and Urea Electrolysis. *ACS Sustain. Chem. Eng.* **2019**, *7*, 10035–10043. [[CrossRef](#)]
51. Chamani, S.; Sadeghi, E.; Unal, U.; Peighambaroust, N.S.; Aydemir, U. Tuning Electrochemical Hydrogen-Evolution Activity of CoMoO₄ through Zn Incorporation. *Catalysts* **2023**, *13*, 798. [[CrossRef](#)]
52. Hao, L.P.; Hanan, A.; Walvekar, R.; Khalid, M.; Bibi, F.; Wong, W.Y.; Prakash, C. Synergistic Integration of MXene and Metal-Organic Frameworks for Enhanced Electrocatalytic Hydrogen Evolution in an Alkaline Environment. *Catalysts* **2023**, *13*, 802. [[CrossRef](#)]
53. Al-Enizi, A.M.; Shaikh, S.F.; Ubaidullah, M.; Ghanem, M.A.; Mane, R.S. Self-grown one-dimensional nickel sulfo-selenide nanostructured electrocatalysts for water splitting reactions. *Int. J. Hydrogen Energy* **2020**, *45*, 15904–15914. [[CrossRef](#)]
54. Wang, T.; Guo, X.; Zhang, J.; Xiao, W.; Xi, P.; Peng, S.; Gao, D. Electronic structure modulation of NiS₂ by transition metal doping for accelerating the hydrogen evolution reaction. *J. Mater. Chem. A* **2019**, *7*, 4971–4976. [[CrossRef](#)]
55. Xiao, X.; Huang, D.; Fu, Y.; Wen, M.; Jiang, X.; Lv, X.; Li, M.; Gao, L.; Liu, S.; Wang, M.; et al. Engineering NiS/Ni₂P Heterostructures for Efficient Electrocatalytic Water Splitting. *ACS Appl. Mater. Interfaces* **2018**, *10*, 4689–4696. [[CrossRef](#)] [[PubMed](#)]
56. Shinde, N.M.; Raut, S.D.; Ghule, B.G.; Deokate, R.J.; Narwade, S.H.; Mane, R.S.; Xia, Q.; Pak, J.J.; Kim, J.-S. Hydrogen Evolution Reaction Activities of Room-Temperature Self-Grown Glycerol-Assisted Nickel Chloride Nanostructures. *Catalysts* **2023**, *13*, 177. [[CrossRef](#)]
57. Ahsan, M.A.; He, T.; Eid, K.; Abdullah, A.M.; Curry, M.L.; Du, A.; Puente Santiago, A.R.; Echegoyen, L.; Noveron, J.C. Tuning the Intermolecular Electron Transfer of Low-Dimensional and Metal-Free BCN/C₆₀ Electrocatalysts via Interfacial Defects for Efficient Hydrogen and Oxygen Electrochemistry. *J. Am. Chem. Soc.* **2021**, *143*, 1203–1215. [[CrossRef](#)]
58. Miao, R.; He, J.; Sahoo, S.; Luo, Z.; Zhong, W.; Chen, S.-Y.; Guild, C.; Jafari, T.; Dutta, B.; Cetegen, S.A.; et al. Reduced Graphene Oxide Supported Nickel–Manganese–Cobalt Spinel Ternary Oxide Nanocomposites and Their Chemically Converted Sulfide Nanocomposites as Efficient Electrocatalysts for Alkaline Water Splitting. *ACS Catal.* **2017**, *7*, 819–832. [[CrossRef](#)]
59. Alobaid, A.; Wang, C.; Adomaitis, R.A. Mechanism and Kinetics of HER and OER on NiFe LDH Films in an Alkaline Electrolyte. *J. Electrochem. Soc.* **2018**, *165*, J3395. [[CrossRef](#)]
60. Cossar, E.; Houache, M.S.E.; Zhang, Z.; Baranova, E.A. Comparison of electrochemical active surface area methods for various nickel nanostructures. *J. Electroanal. Chem.* **2020**, *870*, 114246. [[CrossRef](#)]
61. Zhao, T.; Gao, J.; Wu, J.; He, P.; Li, Y.; Yao, J. Highly Active Cobalt/Tungsten Carbide@N-Doped Porous Carbon Nanomaterials Derived from Metal-Organic Frameworks as Bifunctional Catalysts for Overall Water Splitting. *Energy Technol.* **2019**, *7*, 1800969. [[CrossRef](#)]
62. Doan, T.L.L.; Tran, D.T.; Nguyen, D.C.; Kim, D.H.; Kim, N.H.; Lee, J.H. Rational Engineering Co_xO_y Nanosheets via Phosphorous and Sulfur Dual-Coupling for Enhancing Water Splitting and Zn–Air Battery. *Adv. Funct. Mater.* **2021**, *31*, 2007822. [[CrossRef](#)]
63. Shao, Z.; Vollrath, F. Surprising strength of silkworm silk. *Nature* **2002**, *418*, 741. [[CrossRef](#)] [[PubMed](#)]
64. Kannan, P.; Akshaya, K.B.; Sudhakar, Y.N.; Vijayan, A.; Varghese, A. Amorphous Ru-Pi nanoclusters decorated on PEDOT modified carbon fibre paper as a highly efficient electrocatalyst for oxygen evolution reaction. *Mater. Chem. Phys.* **2021**, *267*, 124650. [[CrossRef](#)]
65. Qu, Y.; Shao, M.; Shao, Y.; Yang, M.; Xu, J.; Kwok, C.T.; Shi, X.; Lu, Z.; Pan, H. Ultra-high electrocatalytic activity of VS₂ nanoflowers for efficient hydrogen evolution reaction. *J. Mater. Chem. A* **2017**, *5*, 15080–15086. [[CrossRef](#)]

Disclaimer/Publisher’s Note: The statements, opinions and data contained in all publications are solely those of the individual author(s) and contributor(s) and not of MDPI and/or the editor(s). MDPI and/or the editor(s) disclaim responsibility for any injury to people or property resulting from any ideas, methods, instructions or products referred to in the content.